SANDIA REPORT
SAND2006-7101
Unlimited Release
Printed November 2006

LDRD Final Report on Si Nanocrystal as Device Prototype for Spintronics Applications

Wei Pan, Roberto G. Dunn, Malcolm S. Carroll, Jason C. Verley, Luke N. Brewer, James C. Banks, Josephine J. Sheng, and Daniel L. Barton

Prepared by
Sandia National Laboratories
Albuquerque, New Mexico 87185 and Livermore, California 94550

Sandia is a multiprogram laboratory operated by Sandia Corporation,
a Lockheed Martin Company, for the United States Department of Energy's
National Nuclear Security Administration under Contract DE-AC04-94AL85000.

Issued by Sandia National Laboratories, operated for the United States Department of Energy by Sandia Corporation.

Available to DOE and DOE contractors from
U.S. Department of Energy
Office of Scientific and Technical Information
P.O. Box 62
Oak Ridge, TN 37831

Telephone: (865) 576-8401
Facsimile: (865) 576-5728
E-Mail: reports@adonis.osti.gov
Online ordering: http://www.osti.gov/bridge

Available to the public from
U.S. Department of Commerce
National Technical Information Service
5285 Port Royal Rd.
Springfield, VA 22161

Telephone: (800) 553-6847
Facsimile: (703) 605-6900
E-Mail: orders@ntis.fedworld.gov
Online order: http://www.ntis.gov/help/ordermethods.asp?loc=7-4-0#online

SAND2006-7101
Unlimited Release
Printed November 2006

LDRD Final Report on Si Nanocrystal as Device Prototype for Spintronics Applications

Wei Pan and Roberto G. Dunn
Semiconductor Materials and Device Sciences Department

Malcolm S. Carroll and Jason C. Verley
Photonic Microsystems Technologies Department

Luke N. Brewer
Materials Characterization Department

James C. Banks
Radiation Solid Interactions Department

Josephine J. Sheng
Radiation-Hard CMOS Technology Department

Daniel L. Barton
Semiconductor Materials and Device Sciences Department

Sandia National Laboratories
P. O. Box 5800
Albuquerque, NM 87185

Abstract

The silicon microelectronics industry is the technological driver of modern society. The whole industry is built upon one major invention -- the solid-state transistor. It has become clear that the conventional transistor technology is approaching its limitations. Recent years have seen the advent of magnetoelectronics and spintronics with combined magnetism and solid state electronics via spin-dependent transport process. In these novel devices, both charge and spin degree freedoms can be manipulated by external means. This leads to novel electronic functionalities that will greatly enhance the speed of information processing and memory storage density. The challenge lying ahead is to understand the new device physics, and control magnetic

phenomena at nanometer length scales and in reduced dimensions. To meet this goal, we proposed the silicon nanocrystal system, because: 1) It is compatible with existing silicon fabrication technologies; 2) It has shown strong quantum confinement effects, which can modify the electric and optical properties through directly modifying the band structure; and 3) the spin-orbital coupling in silicon is very small, and for isotopic pure ^{28}Si, the nuclear spin is zero. These will help to reduce the spin-decoherence channels. In the past fiscal year, we have studied the growth mechanism of silicon-nanocrystals embedded in silicon dioxide, their photoluminescence properties, and the Si-nanocrystal's magnetic properties in the presence of Mn-ion doping. Our results may demonstrate the first evidence of possible ferromagnetic orders in Mn-ion implanted silicon nanoscrystals, which can lead to ultra-fast information process and ultra-dense magnetic memory applications.

Table of Contents

Accomplishments

First, we have successfully grown and characterized silicon nanocrystals. Silicon nanocrystals (Si-ncs) are formed through a combination of high density plasma enhanced chemical vapor deposition (HDP-CVD) of silicon-rich oxides (SRO) followed by phase separation of the SRO into pure Si-nc and stoichiometric oxide during relatively long annealing (1-3 hours) at temperatures between 1000°C to 1200°C. The Si-ncs and SROs are characterized using transmission electron microscopy, Fourier transmission infrared spectroscopy, Rutherford backscattering, Nuclear Reaction Analysis, ellipsometery. The Si-nc growth is studied in a relatively long thermal budget regime compared to most previous reports available in the literature. Morphology, defects within the nanocrystals and size dependence as a function of thickness in the oxide are exaggerated in this regime and are more readily characterized in the longer diffusion length regime. In particular, evidence and implications of solid-phase epitaxial growth of the Si-ncs are observed and the effects of nearby silicon sinks at the surface and the substrate are highlighted with a strong nanocrystal size dependence with position in the oxide. The depletion of the oxides correlates with the nucleation of extended defects in the silicon substrate, which also could pose challenges to integration of the Si-ncs with other silicon devices. In addition, because the Si-ncs depend on local geometries due to local silicon sinks, integration considerations become more complex when trying to target certain nanocrystal sizes in device structures. Finally, there are a number of studies of Si-nc growth using PECVD produced SROs, however, few reports exist on the use of HDP-CVD SROs. This work, therefore, also offers additional experimental details related to the impact of using this different plasma geometry to generate the SROs.

Second, we have carefully studied the photoluminenance (PL) in more than 20 Si-nc samples under different thermal budgets. A very broad PL peak, blue-shifted from the bulk silicon band edge of ~1.1 eV, was observed. What is really surprising is that in our samples the position of PL peak is apparently pinned between ~900-1000 nm, independent of thermal budget. This is very different from previous studies, where the wavelength of PL peak can be tuned from ~ 600 to ~ 900 nm by controlling nanocrystal size. The pinning mechanism is currently unknown, though we speculate that it is probably related to the radiative surface states of Si-ncs. In a further temperature dependent study carried out in a high thermal budget sample, it was observed that the PL intensity showed a non-monotonic temperature dependence, similar to what reported before. Post-annealing in forming gas strengthens this non-monotonic dependence, and the temperature where the PL intensity displays a peak remains roughly the same, ~ 60K. Based on the above observations, we believe that both the quantum confinement effect and the radiative surface states play an important role in PL.

Furthermore, we studied the magneto-photoluminescence in Mn-ion doped Si-ncs. We demonstrate, *for the first time*, evidence of possible ferromagnetism in Mn-ion implanted Si-ncs systems. This could lead to ultra-fast, ultra-dense magnetic memory applications.

Silicon Nanocrystal Growth through Phase Separation of High Density Plasma Chemical Vapor Deposited Silicon-Rich Oxides in the Long Diffusion Length Regime

Introduction

Silicon-rich oxides (SRO) have attracted attention for their use in creating silicon nanocrystals (Si-ncs), which are attractive for their potential to become CMOS compatible memories or light sources [1]. A significant number of publications have focused on characterization of small silicon nanocrystals that show quantum confinement (i.e., diameter < 5 nm). However, characterization of some of the details of the formation of the nanocrystals are limited by the resolution limits of classic electron probe techniques applied to these small structures. We therefore present an examination of a larger size range of silicon nanocrystals (e.g., 1.5 nm < diameter < 10 nm) grown with a range of thermal budgets that covers a longer silicon diffusion length than typically focused on in the recent literature. The study of this longer diffusion length regime highlights some, as of yet, not well reported effects including silicon depletion from the SROs due to local sinks (i.e., the surface and the silicon substrate) as well as clear evidence of solid-phase epitaxy of the nanocrystals leading to facet like growth. There are various approaches to depositing SROs including ever evolving plasma enhanced chemical vapor deposition techniques, which sometimes lead to important differences in the as-deposited films. Plasma enhanced vapor deposition (PECVD) techniques are attractive for their low temperature and ease of integration, however, most studies in the literature in this area have used capacitively coupled systems that operate at higher pressures and are constrained to use oxygen sources that contain either nitrogen or carbon. These NO_x or CO_x sources lead to high concentrations of nitrogen or carbon in the films, respectively. Little has been reported about nanocrystal formation using HDP-CVD SROs, which differentiates itself from previous PECVD techniques through its use of molecular oxygen as the oxygen source. This leads to the films having lower background concentrations of nitrogen or carbon. We report on the Si-nc growth from these SROs and comment on observed differences, which include a significant difference in the Si-O FTIR local mode sensitivity to oxygen content in the SRO.

Characterization of Silicon-Rich Oxides Deposited by HDP-CVD

Silicon-rich oxides of varying thickness and silicon concentration were deposited on 150 mm diameter, <100>, silicon substrates using a commercially available HDP-CVD chamber with top and side power and gas sources as well as an independent bias source at the chuck. Further details about the chamber are described elsewhere [2]. In order to better control deposition rate or throughput, two different SRO deposition conditions were developed. For high deposition rates (~ 9 nm/sec), the chamber pressure was kept at ~5 mtorr while flowing rates of 126, 180, and 90 sccm of argon, oxygen and silane, respectively. The RF power applied during the high deposition rate film was 1700, 2100, and 2000 Watts applied to the top, side and bias supplies. These high deposition rate SROs were backside cooled using He and the temperature was maintained at ~ 450°C. Silicon content in the SROs was increased by decreasing the oxygen flow (i.e., oxygen partial pressure) in the chamber. For more precise control of SRO thickness a low deposition rate film was also examined (~ 1 nm/sec). The chamber pressure for the oxides was kept at 25 mtorr, 150 Watts of RF power was applied, and the process gas flow rates were 350, 20, and 8 sccm of argon, oxygen and silane for nearly stoichometric silicon dioxide, respectively. These lower deposition rate SROs were not backside cooled resulting in an average

deposition temperature of approximately 300°C. Thicknesses of the oxides were measured using ellipsometry, Fig. 1, modeled with the effective medium approximation. Representative sample thicknesses were measured using alternative approaches like SEM cross sections, SIMS and RBS and agreed relatively well with ellipsometry and compared to representative samples measured by RBS or cross section thickness observed with SEM. Uniformity of both recipes was measured by ellipsometry.

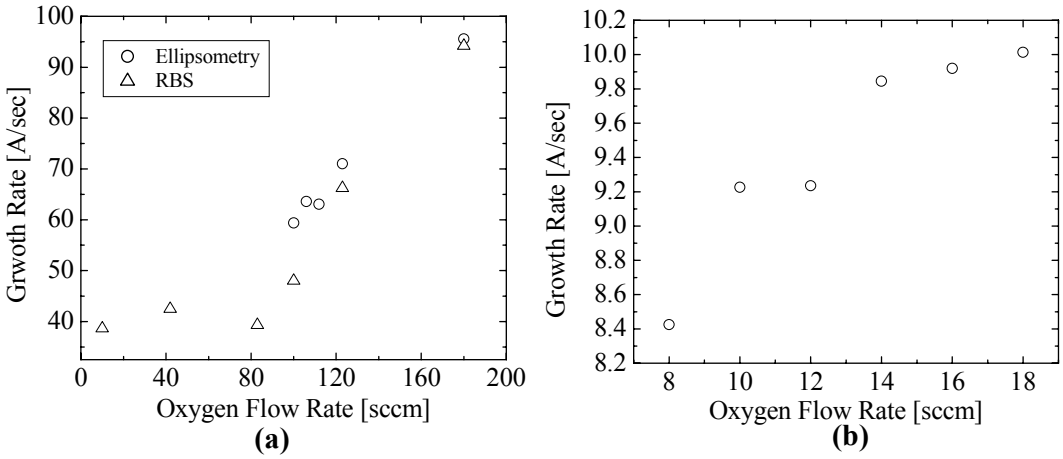

Figure 1 Deposition rates of silicon rich oxides as a function of oxygen flow using both the fast (a) and slow (b) deposition conditions. Thicknesses are measured using ellipsometry and were compared to RBS.

The stoichometric chemical content of the SRO films was measured directly using Rutherford backscattering (RBS) and Elastic Recoil Detection (ERD), Fig 2 (a), (b) & (c). A clear increase in silicon content is observed with decreasing oxygen flow. Presumably the reduction of oxygen flow starves the reacting surface of oxygen to form stoichometric SiO_2 leading to silicon enriched oxide. This process appears to saturate at approximately ~75%, Fig. 2 (a). Simultaneously as oxygen flow is decreased an increase in hydrogen content is also observed by nuclear reaction analysis, Fig. 2 (c). The saturation of silicon content correlates with the presence of very high hydrogen film contents suggesting that hydrogen incorporation replaces the additional silicon incorporation while the oxygen content continues to decrease linearly with oxygen flow. Argon concentrations above an atomic percent are also found, but the argon concentration is not strongly dependent on the oxygen flow. Samples were also examined with RBS and ERD after annealing at temperatures of 1000°C for 60 minutes in argon ambient. The relative oxygen content increases with the removal of hydrogen and argon as a result of the anneals. We infer that this thermal budget, which is smaller or equal to the thermal budgets used to form the silicon nanocrystals in this work, is sufficient to remove hydrogen and argon below RBS detection limits.

The trace chemical background was also measured on representative nearly stoichometric silicon dioxide films (i.e., SiO_2) from both the high and low rate deposition conditions using vapor phase decomposition inductively coupled mass spectrometry (VPD ICP-MS) and Secondary Ion Mass Spectrometry (SIMS). Using VPD ICP-MS a 40 element analysis was done on 25 nm thick oxides before and after all work was done on these SROs. The 40 elements included common metals like Na, K, Mg, Fe, Al, Ni, as well as common elements that are incorporated

into CVD films like, N, C, As, P, Sb and B. All elements other than silicon and oxygen were near or below standard CMOS back-end of the line limits. Aluminum, boron and scandium were elements that were consistently observed above background detection limits at concentrations of approximately $6x10^{10}$ cm^{-2}, $170x10^{10}$ cm^{-2}, $18x10^{10}$ cm^{-2}. We believe the Al and Sc appear at higher concentrations because of the interactions of the plasma with the aluminum-nitride dome within the chamber, while the boron is likely due to cross contamination from high boron content materials commonly being processed in the same chamber. Scandium is a common trace element used in aluminum alloys for stabilization and hardening. The SIMS detection limits were less sensitive than the VPD-ICP method and did not show appreciably larger signals than that detected by VPD-ICP. This indicates that the oxides formed in this chamber have trace elements well below atomic fractions. High concentrations of background elements in oxides are usually necessary to impact the mechanical and optical properties of the oxide. For example, atomic concentrations of phosphorus, boron and erbium (common glass dopants) are necessary to impact the oxide properties like viscosity and luminescence [3]. Furthermore, as previously mentioned, numerous reports of silicon nanocrystal formation using plasma oxides are done with capacitively coupled systems that must operate at higher pressures for which combinations of silane and oxygen are not stable, which leads to high nitrogen (or sometimes carbon) content oxides because N_2O is used instead of pure oxygen to avoid direct reaction between the silane and oxygen at the higher pressure. Mixtures of oxygen and silane are reactively unstable at the higher pressures necessary to spark plasmas in capacitively coupled plasma chambers.

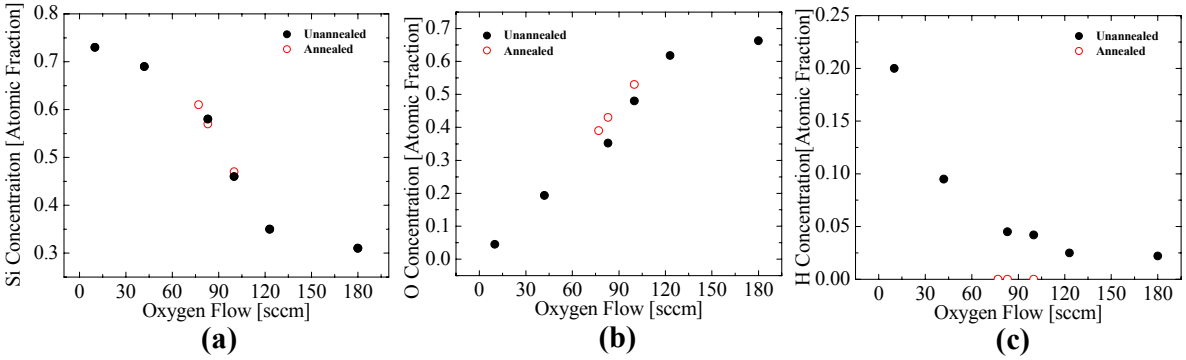

Figure 2 (a) Silicon, (b) oxygen and (c) hydrogen content dependence on oxygen flow in silicon rich oxides produced by high density plasma CVD deposition measured by RBS and ERD.

Rutherford backscattering is not practical for rapid characterization of silicon content in the SRO films, therefore, an alternative approach is desirable. Fourier transform infrared spectroscopy is often used to characterize chemistry within thin films and previous researchers have indicated that oxygen content could be deduced using the peak position of the 1075 cm^{-1} Si-O-Si stretch local vibration [4]. Measurements of absorption strength and position of the Si-O-Si stretch local mode were compared to oxygen concentrations measured by RBS in this work and a linear correlation was observed, Fig. 3. However, a weaker linear dependence of peak position on oxygen content was observed in this work compared to previous reports in PECVD oxides that show a linear decrease to 940 cm^{-1} for 0% oxygen compared to an extrapolated value of ~1010 cm^{-1} at 0% oxygen in this work [4]. A significant difference between the films in this work and those presented earlier is the amount of nitrogen incorporated in the PECVD films or alternatively perhaps the high hydrogen content in the low oxygen concentration films in this

work. We suppose these differences will perturb the elastic properties of the oxide influencing the Si-O-Si stretch mode. Further work is necessary to examine the effects of these other species on the stretch mode but this goes beyond the scope of this study. A linear relationship between thickness and absorption was also found, Fig. 3 (c), indicating that the FTIR may be used as a method to determine thickness of unannealed films as well.

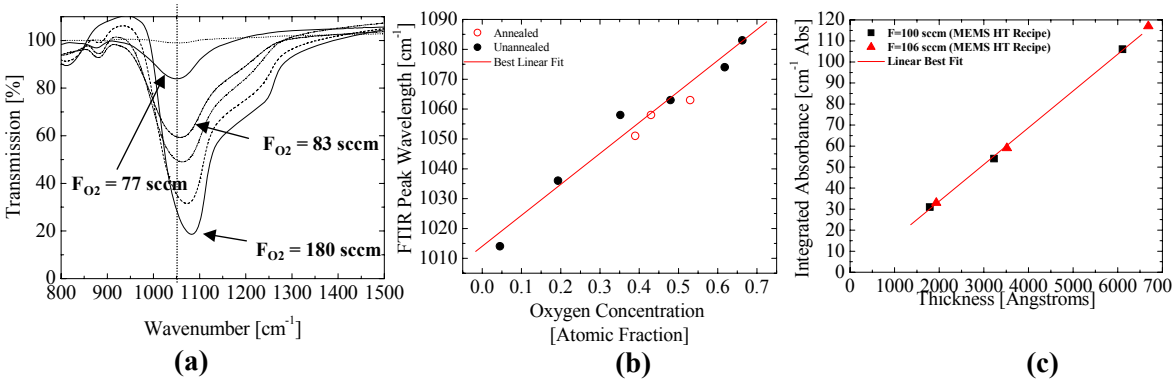

Figure 3 (a) FTIR absorption spectrum of the Si-O-Si stretch local vibrational mode, (b) peak position correlation with oxygen content measured by RBS, and (c) integrated absorption of the stretch mode dependence on thickness of the film.

The optical properties of the SROs like index of refraction also depends on silicon content and is important to characterize especially for optical applications like light emitting diodes and waveguide gain structures. The index of refraction was therefore extracted using ellipsometry, Fig. 4 (a). The dependence of the index of refraction on silicon content can, furthermore, be predicted using the effective medium approximation (EMA) and relatively good agreement between measured index of refraction and silicon content obtained by RBS was found, Fig. 4 (b).

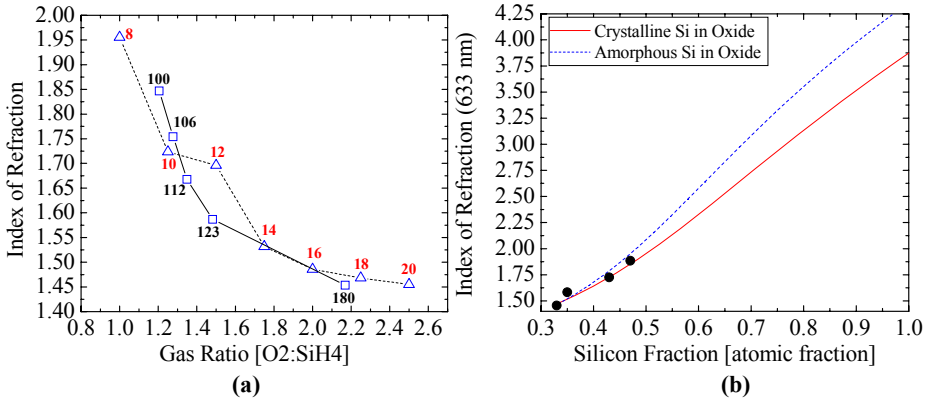

Figure 4 (a) index of refraction as a function of gas flow ratio (flows in sccm of the two different recipes are listed above corresponding points in figure); and (b) comparison of measured index of refraction dependence on silicon content measured by RBS compared to the effective medium approximation prediction.

Formation of Silicon Nanocrystals from Silicon Rich Oxides

Numerous groups have reported that annealing of silicon rich oxides results in phase separation into SiO_2 and silicon clusters. Recently these silicon nanocrystals embedded in oxide and nitride

have gained significant attention because of their luminescence properties both alone [5, 6] and in the presence of rare earth elements like erbium [3, 7] as well as their potential for single electron memories in CMOS [8]. Depending on the annealing conditions and silicon content silicon nanocrystals of diameter of 0 to 10's of nanometers may be formed, Fig 5. Most of the work has focused on a combination of silicon content and annealing conditions that result in small nanocrystals that show quantum confinement. In this paper we focus on analysis of conditions that produce large diameter nanocrystals. The study of these large silicon nanocrystals assists in identifying some of the features of the silicon nanocrystal growth that are not well highlighted in the literature. In particular, analysis of larger nanocrystals with electron probe techniques highlight aspects of the solid phase silicon epitaxy like faceting, Fig 6 (a) and extended defects, Fig 6 (b), that cannot be seen in the smaller nanocrystal studies. Furthermore, the long thermal budgets examined in this work also highlight aspects of the diffusion dominated process such as sinks for the excess silicon that lead to silicon depletion within the oxide, Fig 7, which perturbs the ultimate nanocrystal size.

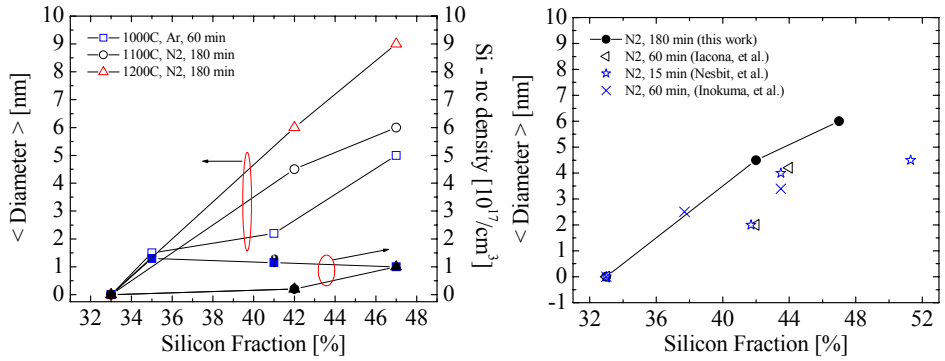

Figure 5 (a) average silicon nanocrystal diameter and density dependence on silicon concentration and annealing condition determined either by TEM or electron energy loss images for this work and (b) a comparison of the sizes measured in this work compared to that reported in the literature for PECVD films.

Silicon-rich oxides with silicon concentrations varying from 33% to 47% were annealed at temperatures from 1000-1200°C from 60 to 180 minutes in either argon or nitrogen. Resulting nanocrystals were subsequently examined using transmission electron microscopy (TEM) and electron energy loss spectroscopy (EELS) and a range of nanocrystal sizes from ~1.5 to 10 nm with a density around 10^{17} cm^{-3} were observed. These average nanocrystal sizes are of the same order of magnitude size as reported elsewhere for annealed PECVD SRO films, Fig. 5 (b). We expect, nevertheless, that some difference in sizes would come from variable silicon diffusivities, dependent on density and impurities, as well as the impact nearby sinks for excess silicon (discussed below) that reduce the available silicon for growing nanocrystals. We also note that there is a relatively large standard deviation in the distribution of nanocrystal size, ~ 6 nm (one standard deviation), leading to the occasional observation of nanocrystals with diameters as large as 30 nm when observing large numbers of nanocrystals as is the case in the low resolution TEM images.

Samples were thinned to roughly 100-200 nm thickness using focused ion beam sputtering. Representative high resolution TEM images, Fig 6, show silicon nanocrystals embedded within the oxide matrix. We conclude that these crystals are silicon for among other reasons, the chemical analysis through EELS indicates high silicon content and because the lattice fringe spacing are consistent with silicon lattice plane spacing.

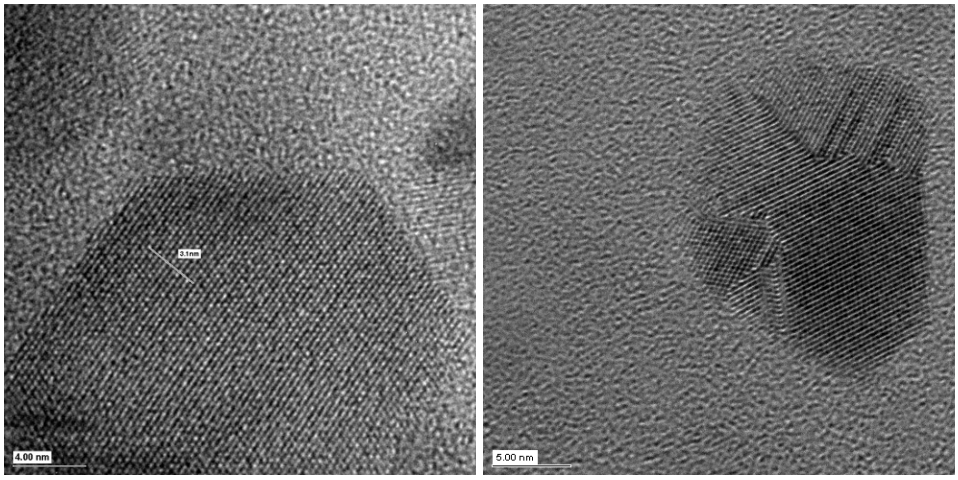

Figure 6 HRTEM of silicon nanocrystals of (a) 47% SRO after 1200°C, 3 hour, N_2 anneal demonstrating clear facet dominated solid phase epitaxial growth and (b) showing in-grown crystal defects.

Several observations may be made from these larger nanocrystal images that are difficult to observe in previous studies of smaller nanocrystals. Some of the larger nanocrystals indicate well defined facets, Fig 6 (a). Facet growth is commonly observed in epitaxay due to differences in densities along different crystal planes, which leads to significant differences in growth rates of different crystal orientations. We assume that the nanocrystal growth occurs through diffusion of excess silicon in the amorphous oxide to the silicon seed after the initial seed nucleation. A purely isotropic diffusion to a seed with a high sticking coefficient and no surface diffusion would result in a spherical nanocrystal. The amorphous oxide has no obvious anisotropy to drive the facet growth, therefore, we suppose that the observed facet growth is due to a non-neglible surface diffusion at the silicon/oxide that permits the kinetics of the different facet growth rates to manifest itself as the faceted nanocrystal. It also stands to reason that for smaller nanocrystals the surface diffusion length is long enough to produce this faceting effect, which suggests that analysis of silicon nanocrystals using the assumption that the nanocrystal is spherical might be improved by taking account of dominant facets like the <111> surface for surface chemistry (e.g., oxygen-silicon bonding) and quantum confinement calculations.

Stacking fault or misaligned poly-grain defects are also observed, representing a subset of the HRTEM imaged nanocrystals, Fig. 6 (b). If we conclude that the growth is epitaxy-like then mechanisms of crystal defect formation are likely similar in origin as what is commonly observed for planar epitaxy except for the occasions when nearby nanocrystals grow together. Two candidates for defect formation during epitaxial growth under these conditions are stacking fault formation due to high levels of oxygen incorporation at the epitaxy growth front, which could be expected within an oxide matrix, or defect formation due to the kinetics of too high a

silicon flux reaching the surface compared to the rate that it can crystallize in the lowest free energy configuration. Very high growth rates are correlated with a transition from epitaxy to poly-crystal growth in planar epitaxy.

Regardless of the mechanism responsible for the defect formation, the presence of crystal defects is of particular relevance to any optical studies of nanocrystals because it is well known that defects like dislocations and oxygen related defects (e.g., oxygen inclusion in ncs, oxygen vacancies, etc.) directly impact both luminescence intensity (i.e., recombination rates) as well as producing their own mid-gap luminescence lines [9]. Photoluminescence from some samples in this work do show evidence of singlet-triplet localization effects due to quantum confinement, deduced from the temperature dependence of the luminescence intensity [10]. However, the luminescence peak energy is not well correlated with size signaling the potential effect of, as of yet, unidentified participation of defects to the PL [11], as we will discuss below.

Diffusion plays a critical role in the phase separation process and therefore dominates the kinetics of determining the nanocrystal size dependence on time [12]. EELS and TEM of the high thermal budget samples shows a second equally important mechanism impacting nanocrystal size, silicon loss to local sinks, Fig 7 & 8. An electron energy loss image shows a map of the relative oxygen concentration measured in a 47% SRO annealed for 3 hours at 1200°C in nitrogen. Average diameter sizes were measured from this and similar images and plotted in a coarse grid as a function of depth in the oxide, Fig 7 (a). Sizes of the nanocrystals decrease in size with proximity to both the oxide surface and the silicon/oxide interface. In this particular case, the SRO film was grown with a 30 nm stoichiometric oxide buffer layer between the silicon and the SRO so no nanocrystals were expected in this region. Nevertheless a silicon depleted region significantly greater than the buffer layer thickness is observed at the Si/oxide interface. A silicon depletion region is also observed at the SiO_2/air interface. The SROs were nominally uniform silicon concentrations, which is confirmed by RBS on representative samples and good ellipsometry fits to films modeled as uniform, therefore, we assume that the non-uniformity in the silicon content is a result of the annealing.

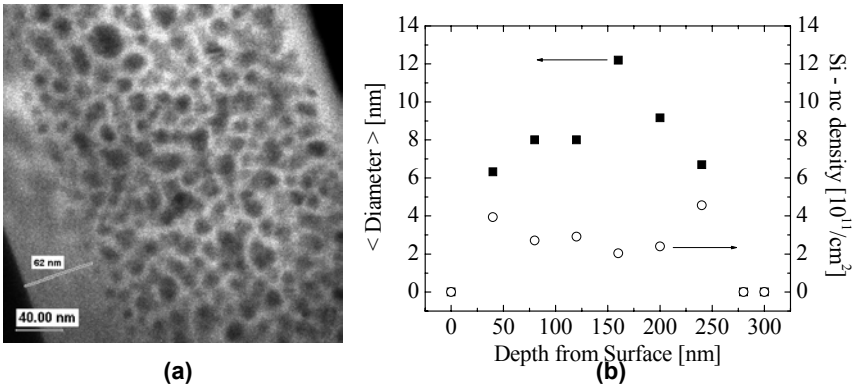

Figure 7 (a)EELS of 1200°C annealed 47% SRO and (b) the average diameter of the nanocrystal as a function of depth from surface.

A hypothesis to explain the silicon depletion regions is that local silicon sinks are present that remove the silicon from the oxide and prevent it from contributing to increasing the size of the nanocrystal. It is well known that Si-O is a volatile species at high temperatures [13, 14] and this would be a very likely candidate for silicon removal from the surface during annealing at high temperatures. It is also reasonable to expect that silicon would condense on the underlying silicon substrate. This effect appears to be exagerated in dramatic fashion in samples annealed at 1200°C in which extended defects (e.g., extra planes of silicon) are observed to nucleate in the silicon substrate that correlate with regions completely depleted of nanocrystal formation, Fig 8. The nucleation of these defects within the silicon are not uniform, but do suggest significant migration of silicon from the oxide into the substrate. This effect is not observed in samples annealed at lower temperatures.

The presence of these silicon sinks has immediate consequences for future design and controlled fabrication of devices using silicon nanocrystals in oxide. Excess silicon condensation within the bulk silicon could lead to detrimental electrical defects for devices and clearly silicon nanocrystal diameters will be affected by the local geometry if measures are not taken to prevent the silicon from out-diffusing such as capping with a diffusion barrier like nitrides.

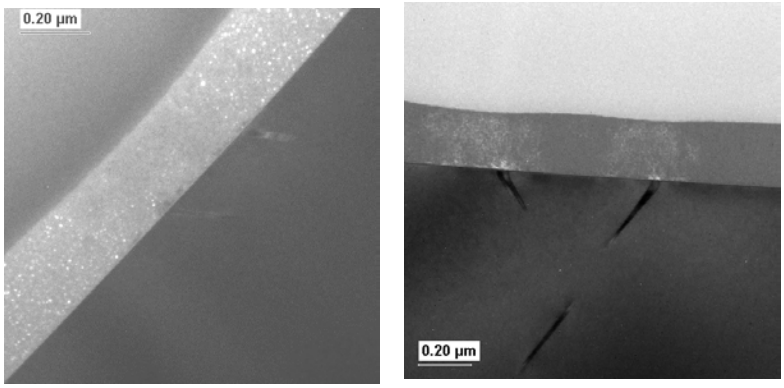

Figure 8, low resolution TEM dark field image of 42% SRO after annealing at 1200°C, 3 hours, N_2 showing (a) a region depleted of silicon nanocrystals and (b) extra silicon planes incorporated into the silicon lattice that correlate with the location of the silicon depleted region.

Summary

Silicon rich oxides were produced using high density plasma chemical vapor deposition (HDP-CVD) and characterized using various techniques to determine the resulting ratios of silicon to oxygen as well as the trace background chemical concentrations. Silicon concentrations from 33% to 70% were produced and background concentrations of over 40 elements were examined finding traces of only aluminum and scandium along with hydrogen, argon and nitrogen that are removed after annealing. The oxygen concentration was furthermore correlated to the position of the FTIR Si-O-Si stretch local mode peak position, which was found to have a different dependence compared to nitrogen rich SROs studied previously. The dependence of the index of refraction on silicon content is furthermore found to agree relatively well with the effective medium approximation.

Silicon nanocrystal formation was subsequently studied by examining various annealing thermal budgets in combination with different silicon concentrations. This work focuses on long diffusion length effects to complement numerous publications focused on producing and characterizing smaller quantum confined silicon nanocrystals. Effects that are highlighted by the study of nanocrystals for longer diffusion length conditions include facet growth, crystal defect formation, and local sinks for excess silicon at the surface and the silicon substrate. In particular, facet growth suggests surface diffusion lengths long enough to produce solid-phase epitaxy like growth, which has implications about possible mechanisms of defect formation in the nanocrystals that are also observed in a sub-set of the imaged nanocrystals. Furthermore, silicon loss out the surface and silicon condensation on and in the silicon substrate have implications for future design and controlled fabrication of nanocrystals suggesting that either silicon diffusion stops may need to be added or alternatively better models of silicon diffusion and nanocrystal growth will be needed to fully exploit this future material system.

Photoluminescence in Silicon-Rich Oxide Thin Films under Different Thermal Treatments

Introduction

In light of future applications in integrated photonic circuits, highly luminescent nanostructured silicon materials, e.g., silicon nanocrystal (Si-nc), have attracted a lot of recent attention [15-19]. In Si-nc materials, due to a strong quantum confinement effect, the momentum conservation rule is expected to be relaxed [20]. Consequently, they can become efficient light emitting materials even with an indirect bandgap. Despite more than one decade of research, yet, the physics of photoluminescence (PL) in Si-ncs remains unsettled [1,6,21-30]. On the one hand, there have been many experiments showing that PL in Si-nc materials is modified by the quantum confinement effect. On the other hand, there have also been experiments in which PL was shown to be related to the radiative interface states, e.g., the Si=O double bonds [22,26].

We examine this problem by doing PL measurements in silicon rich oxide (SRO) thin film samples under different thermal treatments, i.e., from zero thermal budget (ZTB) to high thermal budget (HTB). In more than 20 samples, a very broad PL peak, blue-shifted from the bulk silicon band edge of ~1.1 eV, was observed. What is really surprising is that in our samples the position of PL peak is apparently pinned between ~900-1000 nm (or in the photon energy range of ~ 1.2-1.4 eV), independent of thermal budget [31]. This is very different from previous studies, where the wavelength of PL peak can be tuned from ~ 600 to ~ 900 nm by controlling nanocrystal size [1,6,21-30]. The pinning mechanism is currently unknown, though we speculate that it is probably related to the radiative interface states at the surface of Si-ncs. In a further temperature dependent study carried out in a HTB sample, it was observed that the PL intensity showed a non-monotonic temperature dependence. This non-monotonic temperature dependence has been observed before [21,24], and was attributed to an energy splitting between the excitonic singlet and triplet levels [24], a consequence of quantum confinement effect. Post-annealing in forming gas strengthens this non-monotonic dependence, and the value of the temperature where the PL intensity displays a peak remains roughly the same, ~ 60K. Based on the above observations, we believe that both the quantum confinement effect and the radiative interface states play an important role in PL.

Sample preparation and experimental techniques

The SRO thin films were prepared using plasma assisted chemical vapor deposition and annealing of the SROs, as discussed above. On a [100] silicon wafer, a silicon dioxide buffer layer of 30 nm was first grown. Then a silicon rich oxide (SRO) SiO_x ($x < 2$) thin film of various thickness was deposited using high density plasma enhanced chemical vapor deposition (PECVD) with SiH_4 and pure O_2, which differs from previous reports using typically higher pressure plasma geometries that, for example, require the use of N_2O. The silicon content was controlled by adjusting the O_2 flow rate. It was either determined by Rutherford backscattering (RBS), or through a linear interpolation between two known RBS values. The silicon concentration in the SiO_x varies from 33% (or pure SiO_2) to 77%, the highest ratio in this work. During the sample growth, the substrate temperature was kept below 450 °C.

PL measurements were performed using the 514.5 nm line of argon ion laser. A liquid nitrogen cooled Ge detector and a phase lock-in amplifier at a chopper frequency of 30 Hz were utilized to detect PL signal. Measurement temperatures were from 4 to 300K. A single silicon optical fiber was used to carry pump and luminescence light to and from the samples. No correction for the system response was made in our PL data.

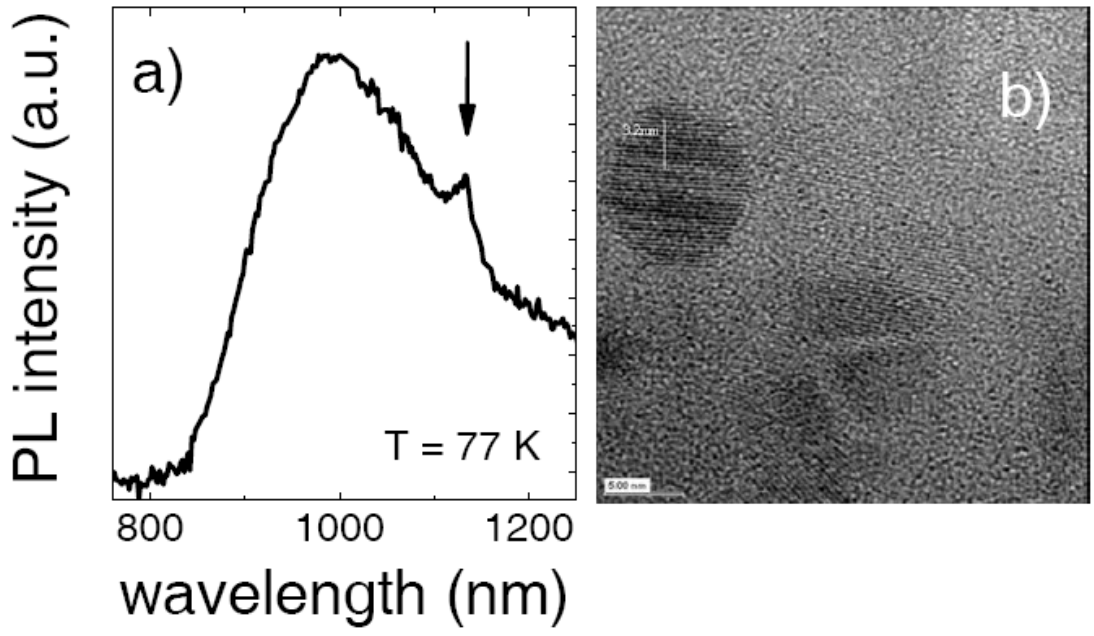

Figure 9 a) Photoluminescence for a high thermal budget sample, sample A, at the temperature of 77 K. A broad peak centered at ~ 1000 nm is clearly seen. The arrow marks the PL peak of the bulk silicon band edge. b) A HRTEM picture of another high thermal budget sample. The average diameter of SiNCs is ~ 5 nm. SiNCs of diameter smaller than 5 nm, some down to ~ 2nm, were also observed.

Experimental results

In Figure 9, we show the PL results for sample A. Sample A has a silicon content of 47 atomic% (at.%), and was annealed in N_2 at 900 °C for 10 minutes. It is expected that during the annealing process the extra silicon will precipitate out of the silicon dioxide matrix and silicon nanocrystals are formed. Indeed, the formation of Si-ncs after annealing was confirmed in high resolution

TEM (HRTEM) measurements. As shown in Fig. 9b, in another 47 at.% SRO sample annealed in N_2 at 1100 °C for 3 hours, the average diameter of Si-ncs is ~ 5 nm. Si-ncs of diameter smaller than 5 nm, down to ~ 2 nm, have also been observed. In sample A, a broad PL peak is seen, centered at the wavelength of ~ 1000 nm, or the photon energy of ~1.2 eV. It is blue-shifted from the bulk silicon band edge of ~1.1 eV, marked by the arrow.

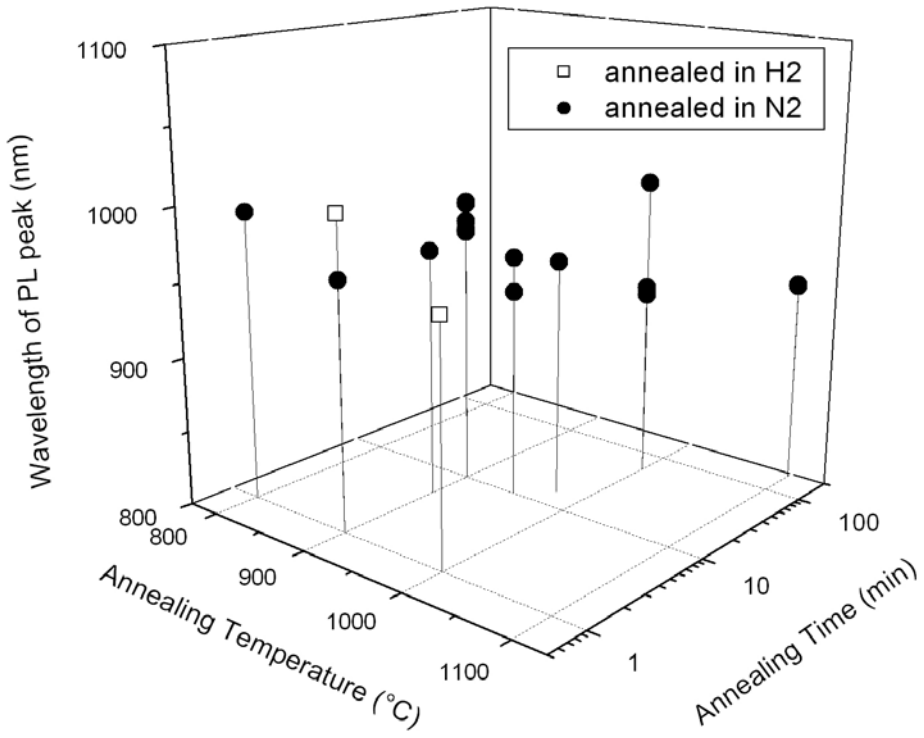

Figure 10 3D plot on the wavelength of photon emission peak versus annealing temperatures (in units of °C) and time (in units of minutes) for 20 HTB samples. Results from zero budget samples are not included.

Different thermal treatments were carried out for more than 20 samples with various silicon contents. In general, the thermal annealing was done in the N_2 environment. To compare, 2 samples were also annealed in the H_2 environment. In Figure 10, we plot the wavelength of PL peak for these samples as a function of annealing temperature and time. For a large parameter space in thermal treatment, the wavelength apparently falls into the range of ~ 900-1000 nm, or in the photon energy range of ~ 1.2 -1.4 eV. Results from three ZTB samples are not included in this plot. Nevertheless, the position of their PL peaks also falls in the same range of ~1.2-1.4 eV.

In an effort to further examine the physical origin of PL in our samples, temperature dependent study was carried out in two specimens, samples A1 and A2, cut side by side from the same wafer of sample A. The difference between A1 and A2 is that sample A2 received an additional post-annealing in forming gas at 410 °C for ~ 5min. In Figure 11, the temperature dependence of the intensity of PL peak is shown for the two samples. It is clearly seen that the PL intensity shows a non-monotonic temperature dependence. For sample A1, the intensity increases slowly when T is increased from 4K. It reaches a maximum at T ~ 60K. Beyond this temperature, the

intensity drops quickly and becomes discernable from the background signal at T ~ 300K. After post-annealing in forming gas, interestingly, the temperature where the intensity reaches the maximal value remains unchanged, ~ 60 K. On the other hand, the non-monotonic dependence becomes stronger. For example, the ratio for the PL intensity between T = 60K and 10K is ~ 1.55 in sample A2, while it is only ~ 1.05 in sample A1.

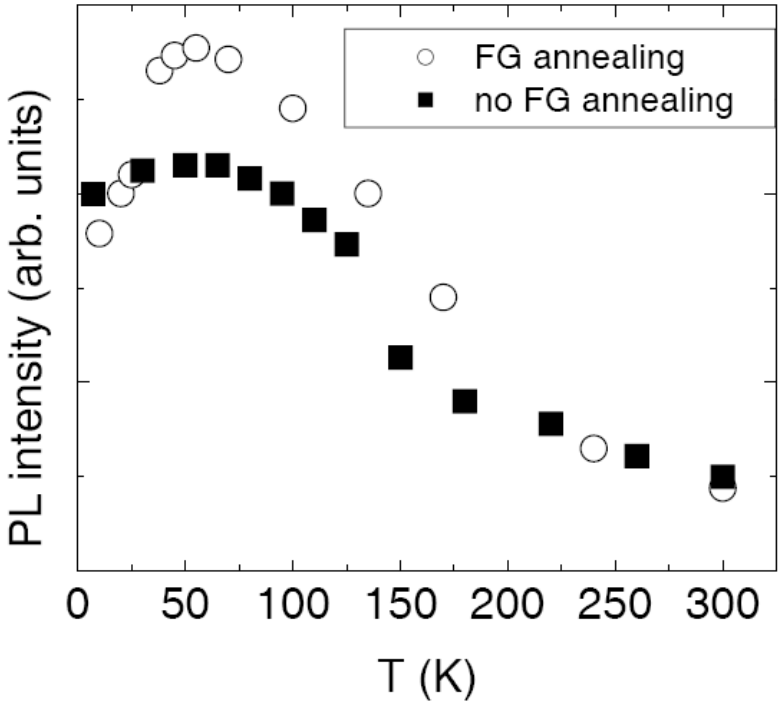

Figure 11 Temperature dependence of the intensity of PL peak in specimens A1 (solid squares) and A2 (open dots). A non-monotonic dependence is observed in both samples.

The pinning of the wavelength of PL peak is unexpected and different from most previous studies [1,6,21-30], where the wavelength of PL peaks can be varied from ~ 600 to ~ 900 nm by varying the nanocrystal sizes. At the present time, it is not known to us what causes the apparent pinning phenomenon. On the other hand, compared to previous reports where SiH_4 and N_2O (or CO_2) were used in PECVD growth, in this work, SiH_4 and pure O_2 were used. Perhaps, use of pure O_2 might introduce a large amount of the Si=O double bonds between the crystalline silicon core and silicon oxide matrix which, in turn, could help to pin the wavelength of PL peak. Indeed, it has been shown that with a maximal oxygen coverage at the surface of Si-ncs, the band gap can fall into the range of ~ 1.2-1.4eV [32]. This hypothesis seems to be able to explain another observation in that the position of PL peak is uncorrelated with silicon content. In previous work, it was shown that under the same thermal treatment, the size of Si-ncs increases with increasing silicon content. As a result, the PL peak red shifts in correlation with increasing silicon content [29]. In Figure 12, we plot the PL trace for three of our samples with silicon content ranging from ~ 39 to 47 at.%. All three samples were annealed in N_2 at 1000 °C for 1 hour. The PL peak first red shifts as the Si content increases from 39 at.% to 42 at.%. However, a further red-shift is not observed as the Si content continues to increase from 42 at.% to 47 at.%. Instead, the PL peak blue shifts to ~ 950 nm. In Fig. 12b, the wavelength of photon emission

peak is plotted as a function of as-grown silicon concentration for 20 HTB samples. Clearly, no correlation is observed between the PL peak position and the silicon concentration. This un-correlation is hard to explain solely by the quantum confinement effect. However, it is consistent with the radiative interface luminescence model where the wavelength of PL peak is pinned and it is natural that the PL peak position and silicon content are not correlated.

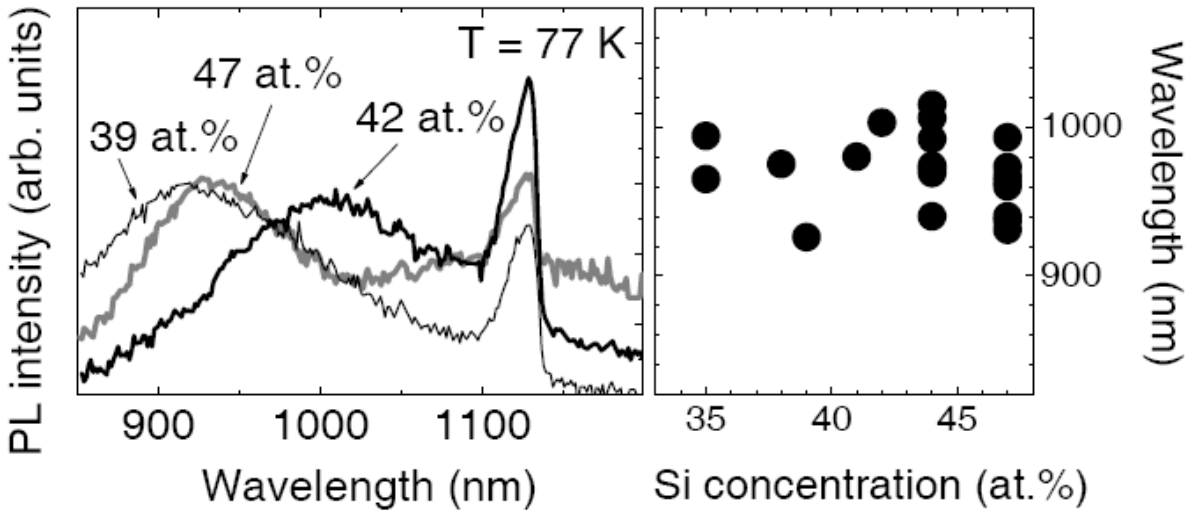

Figure 12 a) PL data for three samples with different silicon content, ranging from ~ 39 at.% to 47 at.%. All three samples were annealed in N_2 at 1000 C for I hour. The measurement temperature is 77K. b) Wavelength of photon emission peak vs. as-grown silicon concentration for 20 high thermal budget samples.

The non-monotonic temperature dependence has been observed before [21,24], and was attributed to an energy splitting between the excitonic singlet and triplet levels [24], a consequence of quantum confinement effect. This, together with the above experimental results -- the blue-shifted PL peak and its wavelength independent of thermal treatment and silicon concentration, seem to suggest that in our Si-nc samples both the quantum confinement effect and the radiative interface states play an important role in PL. To explain the strengthened non-monotonic dependence after post-annealing, we note that post-annealing in forming gas is known to passivate defect states [6,22]. Consequently, the percentage of the contribution from Si-ncs to the PL intensity is increased, and the non-monotonic temperature effect can become stronger. Moreover, passivation of defect states also helps to reduce the energy lever broadening. This, in turn, reduces the mixing effect between the singlet and triplet levels. As a result, the non-monotonic dependence is also expected to become stronger.

Summary

We have looked at more than 20 samples under different thermal treatments, ranging from zero to the summit thermal budge. In all the samples, a very broad PL peak is observed in the photon energy range of ~ 1.2-1.4 eV, apparently independent of thermal budget. Furthermore, a study of temperature dependent PL was carried out, and a non-monotonic temperature dependence of PL intensity was observed. Based on the above experimental observations, we propose that in our silicon nanocrystal materials both the quantum confinement effect and the radiative interface states at the surface of Si-ncs play an important role in determining the final photoluminescence.

Magneto-Photoluminescence of Mn-Doped Silicon-Rich Silicon Oxide Thin Film

Introduction

It has become clear that the conventional silicon transistor technology is approaching its limitations. New device physics is needed for next generation information process and storage. In recent years, it has witnessed the advent of magnetoelectronics and spintronics, in which one can combine magnetism and solid state electronics via spin-dependent transport process [33,34]. The conventional electronics devices move electronic charge around. In these novel spintronic devices, both charge and spin degree freedoms can be manipulated. Spintronic devices have the potential to operate at considerably higher speeds and consume less power. Of course, before the spintronc device can take off as a viable industry, we have to answer the following questions: Can we combine ferromagnetic metals and semiconductors in integrated circuits? If yes, can we make magnetic semiconductor devices that work at room temperature?

Among the many approaches of combining magnetic ions and semiconductors, the dilute magnetic semiconductor of epitaxially grown III-V semiconductor, $Ga_{1-x}Mn_xAs$, has attracted the most attention. A Curie temperature of as high as 150 K has been achieved in this material system [35]. However, for real applications, any device has to be able to function at room temperature. A critical hurdle to producing spintronic devices that operate at room temperature is to maintain the spin polarization and coherence. Recently, an above room temperature ferromagnetism in Mn-ion implanted silicon (Si) has been demonstrated [36]. This result is very stimulating because it suggests that a critical component for spin based field effect transistors (FET) may be achievable in silicon, making it better suited for spin dependent transport process.

Here, we wish to report preliminary experimental results in the Mn-ion doped Si-nanocrystals (Si-ncs) embedded in silicon rich oxide (SRO). The Si-nanocrystal material system is chosen because: 1) It is compatible with existing silicon fabrication technologies; 2) It has shown strong quantum confinement effects, which can modify the electric and optical properties through directly modifying the band structure. Indeed, in photoluminescence studies, we observed, at the temperature (T) of ~ 4 K, a broad PL peak centered at ~ 1.2 eV. It is blue-shifted from ~ 1.1 eV, the band edge emission for bulk silicon. In the subsequent T-dependent PL study, at zero magnetic (B) field, the PL intensity first increases very slowly and reaches a maximum at T ~ 40 K. Then, the temperature dependence takes a turn and the intensity decreases as T is further increased. At a non-zero B field of B = 0.5 Tesla, the peak temperature (T_{peak}), where the PL intensity reaches its maximum, is higher, at ~ 80-100 K. Furthermore, compared to that at B = 0, the decreasing rate of intensity beyond T_{peak} is much weaker. We speculate that these quantitatively different behaviors between B = 0 and 0.5 Tesla might be due to the ferromagnetism in Mn-ion doped Si-ncs.

Experimental results

SRO thin films have been deposited using high density Plasma Enhanced Chemical Vapor Deposition (HDP-CVD). As shown in the left panel of Figure 13, on a [100] commercially available wafer, a thin layer of silicon oxide is thermally grown. After this buffer layer, HDP-CVD is utilized to deposit SRO, with layer thicknesses controllable to sub-nanometer precision. The Mn-ion implantation was done with multiple energies and fluences: 40 keV to 2×10^{15}

at/cm^2; 100 keV to 4×10^{15} at/cm^2, and 300 keV to 1×10^{16} at/cm^2. Thus, the total implant dose is 1.6×10^{16} at/cm^2. The expected depth profile is shown in the right panel of Fig. 13, with multiple Mn-ion peaks in distributions.

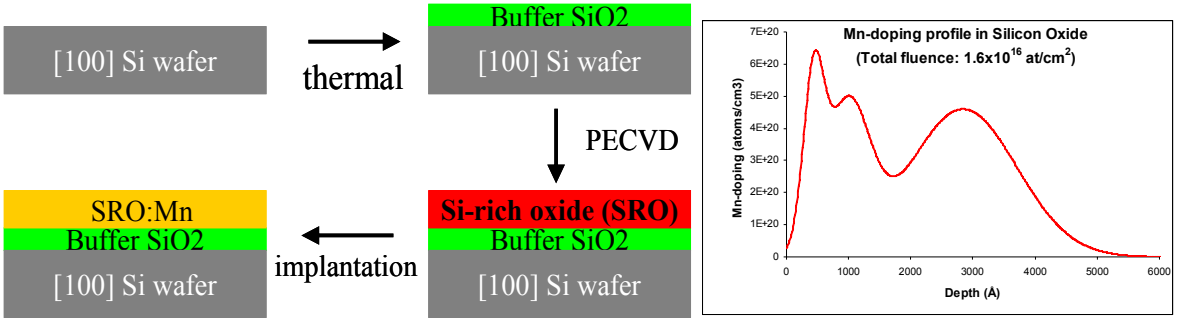

Figure 13 Left -- process of depositing silicon rich oxide (SRO), and Mn-ion implantation. Right -- the expected depth profile of implantation.

PL measurements were performed in a Mn-ion implanted SRO (SRO:Mn) thin film. Result is shown in Figure 14. It is clearly seen that a broad PL peak is centered at ~1.2 eV, blue-shifted from ~1.1 eV of the band edge emission for bulk silicon. For this broad peak, the full width at half maximum is ~ 0.2 eV.

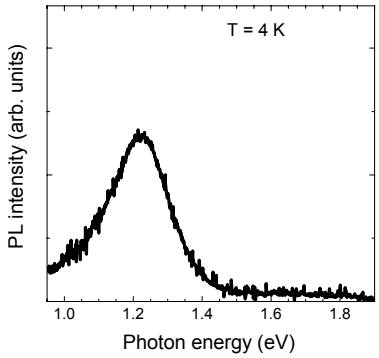

Figure 14 PL measurements for a Mn-ion implanted silicon rich oxide thin film at T ~ 4 K.

Having observed the modified optical properties in this SRO:Mn thin film, we carried out temperature dependent PL studies at different magnetic fields. In the left panel of Figure 15, we show the PL intensity as a function of T, measured at zero B field. At low temperatures, the

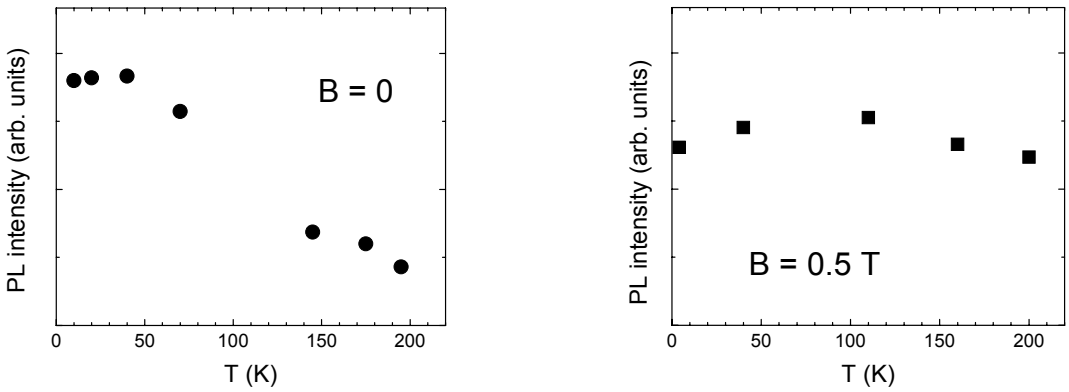

Figure 15 PL intensity versus temperature at B = 0 (left panel), and B = 0.5 Tesla (right panel). The vertical scale is the same for the two panels.

intensity increases, while very slowly, as T is increased. It reaches a maximal value at T ~ 40 K, and then starts to decrease as T is further increased. In the right panel, the temperature dependence was repeated, however, at a non-zero B field of 0.5 Tesla. Compared to the zero B case, again, a non-monotonic T dependence is observed. However, T_{peak} is higher in this case, at ~ 80-100 K. Furthermore, the decreasing rate beyond T_{peak} is much weaker.

In Figure 16, we show the photon energy (E_g), where the PL spectrum displays a peak, as a function of T at B = 0 and 0.5 Tesla, respectively. Both cases show an E_g decrease as T is increased. However, at B = 0, the T dependence of E_g seems to follow the trend in crystalline silicon [37], while at B = 0.5 Tesla, the decrease is roughly linear with T.

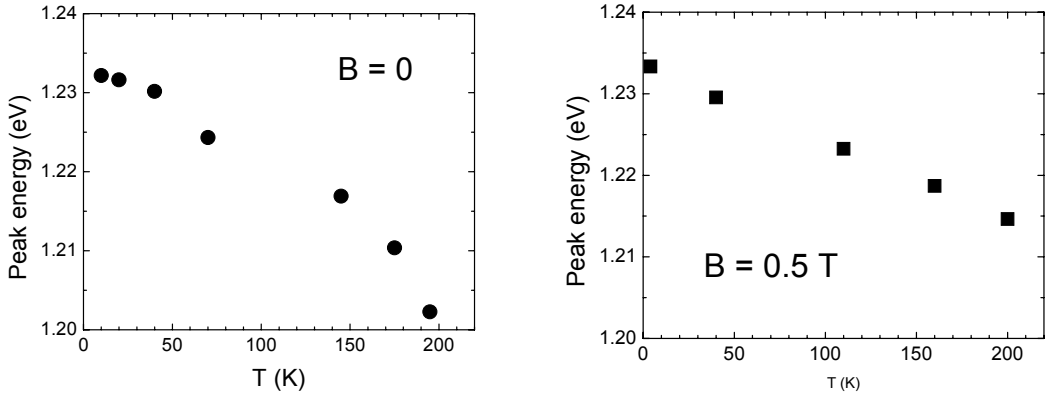

Figure 16 Energy of PL peak versus temperature at B = 0 (left), and B = 0.5 Tesla (right).

Discussion
A blue-shifted PL peak from the bulk silicon band gap has been seen before in previous experiments in nanostructured silicon [15]. We believe that the broad peak at ~ 1.2 is probably due to the formation of Si-ncs in our Mn-ion implanted SRO thin film. Based on this assumption and the peak position, we estimate [26] that the average diameter of Si-ncs is about ~ 5 nm. The assignment of Si-nc origin is further buttressed by the observed non-monotonic temperature dependence of PL intensity [24] and the zero-field temperature dependence of E_g [29]. It has been shown that a non-monotonic dependence of PL intensity can be attributed to an energy splitting between the excitonic singlet and triplet levels, due to the electron-hole exchange interaction, inside of a Si-nc [24].

It is interesting to note that the PL intensity shows quantitatively different T dependent behavior and a larger T_{peak} even with a relatively small B field of 0.5 Tesla. In Ref. [24], it was shown that the value of T_{peak} was also related to the separation between the excitonic singlet and triplet levels. Adding a magnetic field can change this separation. However, with a field of 0.5 Tesla, for crystalline silicon, the Zeeman splitting is ~ 1 K, which is too small to account the change of ~ 40-60 K in T_{peak}. On the other hand, we note that, recently, an above room temperature ferromagnetism in Mn-ion implanted silicon has been demonstrated [36]. Perhaps, the Si-ncs in our thin film sample contain Mn-ions and the so-formed Si-nc:Mn is also ferromagnetic. If this is the case, the enhanced magnetization may be responsible for the enhanced T_{peak} at B = 0.5 Tesla. Of course, more experiments, especially the magneto-PL at much higher B fields, are needed to test our hypothesis.

Summary
We have shown the temperature dependence data of PL in a Mn-ion implanted silicon rich oxide thin film, at zero magnetic field and at B = 0.5 Tesla. Quantitatively different behaviors were observed at these two fields. We speculate that the difference is probably due to the ferromagnetic ordering in Mn doped silicon nanocrystals.

Prospects for future silicon nanocrystal applications

This project proposes to fabricate and study novel prototype devices for next generation light emitters, and information process and storage. The challenge lying ahead is to understand and control quantum confinement effect, magnetic and spin phenomena on very small length scales and in reduced dimensions.

One area that has been growing important and in which Si-ncs may play an important role is to use spintronics devices as sensors. Applications of these sensors are increasingly found in automotive, medical and defense products, and are expected to be important in homeland security applications. As an example, the ability of detecting small amount of magnetic field by utilizing the spin-dependent tunneling process can find potential applications in detecting submarines. Our demonstration of possible ferromagnetic order in Mn-ion doped Si-ncs may represent a significant step towards developing room temperature spintronic devices. It will unleash many more types of devices made possibly by semiconductor high quality optical properties and their ability to amplify both optical and electrical signals, for example, ultra-fast switches and ultra-sensitive sensors.

Successful demonstration of spintronic devices is also of great interest in the strategic areas of secure and fast telecommunication. At the same time, it gives us ample opportunities for investigations of novel quantum transport effects. This research project is closely aligned with the nanoelectronics and photonics thrust area of CINT. By nurturing this science and then harnessing it for spintronics technology systems, we can achieve a differentiating advantage for decades out.

We are grateful to Dr. Y.Q. Wang of LANL for his help on Mn-ion implantation.

References

1. F. Iacona, G. Franzo, and C. Spinella, "Correlation between luminescence and structural properties of Si nanocrystals," *Journal of Applied Physics*, vol. 87, pp. 1295, 2000.
2. HDP-CVD, Applied Materials.
3. D. Pacifici, A. Irrera, G. Franzo, M. Miritello, F. Iacona, and F. Priolo, "Erbium--dopded Si nanocrystals: optical properties and electroluminescent devices," *Physica E*, vol. 16, pp. 331, 2003.
4. P. G. Pai, S. S. Chao, Y. Takagi, and G. Lucovsky, "Infrared spectroscopic study of SiOx films produced by plasma enhanced chemical vapor deposition," *J. Vac. Sci. Technol. A*, vol. 4, pp. 689, 1985.
5. C. Garcia, B. Garrido, P. Pellegrino, R. Ferre, J. A. Moreno, L. Pavesi, M. Cazzanelli, and J. R. Morante, "Absorption cross-sections and lifetimes as a function of size in Si nanocrystals embedded in SiO2," *Physica E*, vol. 16, pp. 429, 2002.
6. K. S. Min, K. V. Shcheglov, C. M. Yang, H. A. Atwater, M. L. Brongersma, and A. Polman, "Defect-related versus excitonic visible light emission from ion beam synthesized Si nanocrystals in SiO2," *Applied Physics Letters*, vol. 69, pp. 2033, 1996.
7. P. G. Kik and A. Polman, "Exciton-erbium interactions in Si nanocrystal-doped SiO2," *Applied Physics Letters*, vol. 88, pp. 1992, 2000.
8. G. Ammendola, M. Vulpio, M. Bileci, N. Nastasi, C. Gerardi, G. Renna, I. Crupi, G. Nicotra, and S. Lombardo, "Nanocrystal metal-oxide-semiconductor memories obtained by chemical vapor deposition of Si nanocrystals," *Journal of Vacuum Science and Technology B*, vol. 20, pp. 2075, 2002.
9. R. Sauer, J. Weber, J. Stolz, E. R. Weber, K.-H. Kusters, and H. Alexander, "Dislocation-related photoluminescence in silicon," *Applied Physics A: Materials Science & Processing*, vol. 36, pp. 1, 1984.
10. M. L. Brongersma, P. G. Kik, A. Polman, K. S. Min, and H. A. Atwater, "Size-dependent electron-hole exchange interaction in Si nanocrystals," *Applied Physics Letters*, vol. 76, pp. 351, 2000.
11. W. Pan, R. Dunn, M. S. Carroll, L. Brewer, and J. Banks, preprint, submitted (2006).
12. L. A. Nesbit, "Annealing characteristics of Si-rich SiO2 films," *Applied Physics Letters*, vol. 46, pp. 38, 1984.
13. J. J. Lander and J. Morrison, *J. Appl. Phys.*, vol. 33, pp. 1300, 1982.

14. F. W. Smith and G. Ghidini, "Reaction of Oxygen with Si(111) and (100): Critical Conditions for the Growth of SiO_2," *J. Electrochem. Soc.*, vol. 128, pp. 1300, 1982.
15. L.T. Canham, Appl.Phys. Lett. 57, 1046 (1990).
16. D. Kovalev, H. Heckler, G. Polisski, and F.Koch, Phys. Stat. Sol. B 215, 871 (1999).
17. L. Pavesi, L. Dal Negro, C. Mazzoleni, G. Franzo, and F. Priolo, Nature 408, 440 (2000).
18. A. Polman, Nature Materials 1, 10 (2002).
19. P.M. Fauchet, Topics in Applied Physics 94, 177 (2004).
20. M.S. Hybertsen, Phys. Rev.Lett. 72, 1514 (1994).
21. Y. Kanemitsu, Phys. Rev. B 53, 13515 (1996).
22. M.L. Brongersma, A. Polman, K.S. Min, E. Boer, T. Tambo, and H.A. Atwater, Appl. Phys. Lett. 72, 2577 (1998).
23. M.V. Wolkin, J. Jorne, P.M. Fauchet, G. Allan, and C, Delerue, Phys. Rev. Lett. 82, 197 (1999).
24. M.L. Brongersma, P.G. Kik, A. Polman, K.S. Min, and H.A. Atwater, Appl. Phy. Lett. 76, 351 (2000).
25. G. Ledoux, O. Guillois, D. Porterat, C.Reynaud, F.Huisken, B.Kohn, and V. Paillard, Phys. Rev. B 62, 15942 (2000).
26. A. Puzder, A.J. Williamson, J.C. Grossman, and G. Galli, Phys. Rev. Lett. 88, 097401 (2002).
27. M. Lopez, B. Garrido, C. Garcia, P. Pellegrino, A. Perez-Rodriguez, J.R. Morante, B. Bonafos, M. Carrada, and A. Claverie, Appl. Phys. Lett. 80, 1637 (2002).
28. J.S. Biteen, N.S. Lewis, H.A. Atwater, A. Polman, Appl. Phys. Lett. 84, 5389 (2004).
29. X.X. Wang, J.G. Zhang, L. Ding, B.W. Cheng, W.K. Ge, J.Z. Yu, and Q.M. Wang, Phys. Rev. B 72, 195313 (2005).
30. A. Tewary, R.D. Kekatpure, and M.L. Brongersma, Appl. Phys. Lett. 88, 093114 (2006).
31. This pinning effect has also been observed before. See, for example, Y. Kanemitsu, H. Uto, Y. Masumoto, T. Matsumoto, T. Futagi, and H. Mimura, Phys. Rev. B 48, 2827 (1993). There the PL peaks occur at ~ 750 nm.
32. A. Puzder, A.J. Williamson, J.C. Grossman, and G. Galli, J. Chem. Phys. 117, 6721 (2002).
33. S.A. Wolf**,** D.D. Awschalom, R.A. Buhrman, J.M. Daughton, S. von Molnár, M.L. Roukes, A.Y. Chtchelkanova, and D.M. Treger, Science **294**, 1488 (2001).
34. S. von Molnár and D. Read, Proc. IEEE **91**, 715 (2003).
35. H. Ohno, D. Chiba, F. Matsukura, T. Omiya, E. Abe, T. Dietl, Y. Ohno, K. Ohtani, Nature **408**, 944 (2000).
36. M. Bolduc, C. Awo-Affouda, A. Stollenwerk, M.B. Huang, F.G. Ramos, G. Agnello, and V.P. LaBella, Phys. Rev. B **71**, 033302 (2005).
37. P.Y. Yu and M. Cardona, Fundamentals of semiconductors (Springer-Verlag, Belin, 1996).

Appendix I: List of refereed publications and presentations

Publications

1. W. Pan, R.G. Dunn, M.S. Carroll, and Y.Q. Wang, *Experimental Studies of Photoluminescence in Mn-Ion Implanted Silicon Rich Oxide Thin Film,* MRS Symposium Proceedings, Volume 910, Page A08-08.

2. M.S. Carroll, L. Brewer, J.C. Verley, J. Banks, J.S. Sheng, W. Pan, R. Dunn*, Silicon Nanocrystal Growth through Phase Separation of High Density Plasma Chemical Vapor Deposited Silicon Rich Oxides in the Long Diffusion Length Regime,* preprint, submitted.

3. W. Pan, R. Dunn, M. S. Carroll, L. Brewer, and J. Banks, *Photoluminescence in silicon rich oxide thin films under different thermal treatments,* preprint, submitted.

Conference Presentations

1. W. Pan, M. S. Carroll, R. G. Dunn, *Photoluminescence in Silicon Rich Silicon Oxide Thin Films,* Spring MRS Meeting, 4/17-21/2006, San Francisco, CA.

2. M. S. Carroll, W. Pan, L. Brewer, J. Verley, J. Banks, R. Dunn, T. Headley, "*Squeezed Silicon Nanocrystals in SiOx/Si3N4 Superlattices Grown with High Density Plasma Chemical Vapor Deposition*", American Vacuum Society meeting (New Mexico chapter), Albuquerque, 2005

Distribution

1	MS 0123	LDRD Office, 0123
1	MS 1082	Malcolm Carroll, 01725
1	MS 1077	J.J. Sheng, 01748
1	MS 1141	Luke Brewer, 01822
1	MS 1082	J. C. Verley, 01725
1	MS 1056	James Banks, 01111
1	MS 1086	Wei Pan, 01123
1	MS 1415	Mark Lee, 01123
1	MS 1415	Ken Lyo, 01123
1	MS 1086	Eric Jones, 01123
1	MS 1415	Eric Shaner, 01123
1	MS 1056	Edward Bielejec, 01111
1	MS 1303	Michael Lilly, 01132
1	MS 1304	John Sullivan, 01132
1	MS 1415	Julia Hsu, 01114
1	MS 1086	Jeff Cederberg, 01126
1	MS 1086	Dan Barton, 01123
1	MS 1415	Charles Barbour, 01120
1	MS 1421	Jerry Simmons, 01130
1	MS 1421	George Samara, 01130
1	MS 1427	Julia Phillips, 01100
2	MS 9018	Central Technical Files, 8944
2	MS 0899	Technical Library, 4536